



## **Brønderslev Hybrid Solar Power Plant Performance Analysis and Monitoring Report**

**Jensen, Adam R.; Furbo, Simon; Perers, Bengt**

*Publication date:*  
2020

*Document Version*  
Publisher's PDF, also known as Version of record

[Link back to DTU Orbit](#)

*Citation (APA):*  
Jensen, A. R., Furbo, S., & Perers, B. (2020). *Brønderslev Hybrid Solar Power Plant: Performance Analysis and Monitoring Report*. Technical University of Denmark, Department of Civil Engineering. BYG Report No. R-449

---

### **General rights**

Copyright and moral rights for the publications made accessible in the public portal are retained by the authors and/or other copyright owners and it is a condition of accessing publications that users recognise and abide by the legal requirements associated with these rights.

- Users may download and print one copy of any publication from the public portal for the purpose of private study or research.
- You may not further distribute the material or use it for any profit-making activity or commercial gain
- You may freely distribute the URL identifying the publication in the public portal

If you believe that this document breaches copyright please contact us providing details, and we will remove access to the work immediately and investigate your claim.

BYG R-449  
December 2020

# **Brønderslev Hybrid Solar Power Plant**

Performance Analysis and Monitoring Report

**Adam R. Jensen, Simon Furbo & Bengt Perers**



**Brønderslev Hybrid Solar Power Plant**  
Performance Analysis and Monitoring Report

Report  
2020

By  
Adam R. Jensen, Simon Furbo & Bengt Perers

Copyright:      Reproduction of this publication in whole or in part must include the customary bibliographic citation, including author attribution, report title, etc.

Cover photo:    Aerial view of the solar collector field and biomass plant in the background.

Published by:   DTU, Department of Civil Engineering, Brovej, Building 118, 2800 Kgs. Lyngby  
Denmark  
[www.byg.dtu.dk](http://www.byg.dtu.dk)

ISBN:            87-7877-550-7

Byg report:     R-449



# Table of Contents

1.	Introduction.....	6
1.1	System overview .....	6
1.2	Solar collector field.....	7
2.	Performance assessment .....	8
2.1	Overall system performance .....	8
2.2	Solar collector field thermal performance .....	11
2.3	Tracking error test .....	12
2.4	Direct radiation sensor soiling .....	13
3.	Solar Field Performance Characterization .....	14
4.	Simulation model.....	19
4.1	Model description .....	19
4.2	Model validation .....	22
4.3	Impact of row distance and axis orientation .....	25
	References .....	28

# Nomenclature

Quantity	Symbol	Unit
Aperture area of collector	$A$	$m^2$
Heat loss coefficient	$\alpha_1$	$W m^{-2} K^{-1}$
Temperature dependence of heat loss coefficient	$\alpha_2$	$W m^{-2} K^{-2}$
Wind speed dependence of heat loss coefficient	$\alpha_3$	$J m^{-3} K^{-1}$
Sky temperature dependence of heat loss coefficient	$\alpha_4$	-
Effective thermal capacity	$\alpha_5$	$J m^{-2} K^{-1}$
Wind speed dependence of peak collector efficiency	$\alpha_6$	$m^{-1} s$
Wind speed dependence of infrared radiation exchange	$\alpha_7$	$W m^{-2} K^{-4}$
Radiation losses	$\alpha_8$	$W m^{-2} K^{-4}$
First order incidence angle modifier coefficient	$b_1$	-
Second order incidence angle modifier coefficient	$b_2$	-
Specific heat capacity of the heat transfer oil	$c_{p,oil}$	$J kg^{-1} K^{-1}$
Specific heat capacity of water	$c_{p,water}$	$J kg^{-1} K^{-1}$
Longwave irradiance	$E_L$	$W m^{-2}$
Fraction of recirculated flow on the secondary side	$f_{recirculation}$	-
Hemispherical solar irradiance	$G$	$W m^{-2}$
Beam irradiance	$G_b$	$W m^{-2}$
Diffuse irradiance	$G_d$	$W m^{-2}$
Incidence angle modifier for diffuse solar irradiance	$K_d$	-
Incidence angle modifier for direct solar irradiance	$K_b(\theta)$	-
Overall heat transfer coefficient of the heat exchanger	$k$	$W m^{-2} K^{-1}$
Mass flow rate through the collector field (primary side)	$\dot{m}_{csp}$	$kg s^{-1}$
Mass flow rate to/from the district heating network	$\dot{m}_{dh}$	$kg s^{-1}$
Mass flow rate on the secondary side of the heat exchanger	$\dot{m}_{dh,hx}$	$kg s^{-1}$
Setpoint for the district heating temperature	$T_{dh,out,set}$	$^{\circ}C$
Temperature of the water from the district heating grid	$T_{dh,in}$	$^{\circ}C$
Setpoint for the solar collector outlet temperature	$T_{csp,out,set}$	$^{\circ}C$
Inlet temperature to the solar collector field	$T_{csp,in}$	$^{\circ}C$
Thermal power output of collector field	$\dot{Q}$	$W$
Thermal power transferred in heat exchanger	$\dot{Q}_{hx}$	$W$
Air speed	$u$	$m s^{-1}$
Peak collector efficiency based on $G_b$	$\eta_{0,b}$	-
Mean temperature of heat transfer fluid	$\vartheta_m$	$^{\circ}C$
Ambient air temperature	$\vartheta_a$	$^{\circ}C$
Longitudinal incidence angle	$\theta_L$	$^{\circ}$
Transversal incidence angle	$\theta_T$	$^{\circ}$
Stefan- Boltzmann constant	$\sigma$	$W m^{-2} K^{-4}$

# 1. Introduction

In 2018 Brønderslev Forsyning inaugurated the world's first power plant which combines concentrated solar power (CSP) and a biomass boiler to generate electricity using an Organic Rankine Cycle (ORC) turbine and utilizing the waste heat for district heating. This report presents an analysis of the monitoring results of the combined heat and power plant's first three years of operation, as well as a simulation model of the system.

First, an overview of the power plant is given in Section 1.1 and the solar collector field is described in detail in Section 1.2. Next, the monitoring results for the overall plant are given in Section 2, primarily focusing on the solar collector field. The performance of the solar collector is characterized in Section 3. Finally, in Section 4 a simulation model for the solar collector field is developed, validated, and used to investigate the impact of row spacing and collector field orientation.

## 1.1 System overview

The Brønderslev hybrid plant is a combined heat and power (CHP) plant inaugurated in 2018 and supplies district heating to the town Brønderslev in Northern Jutland, Denmark (latitude: 57.255 °N, longitude: 9.955 °E). The plant integrates two methods to heat thermal oil parallel: a 16.6 MW solar field and two 10 MW biomass boilers. The hot thermal oil is supplied to an Organic Rankine Cycle (ORC) turbine which generates electricity and supplies heat to the local district heating grid. To achieve as high an efficiency as possible, the flue gas is used as a heat source for two heat pumps which preheats the district heating water to the ORC. Additionally, a third heat pump utilizes the warm air in the plant as a heat source. The total price for the plant and solar collector field was approximately €44 million, of which €2.7 million was granted by the Danish Department of Energy's Energy and Demonstration Program (EUDP).

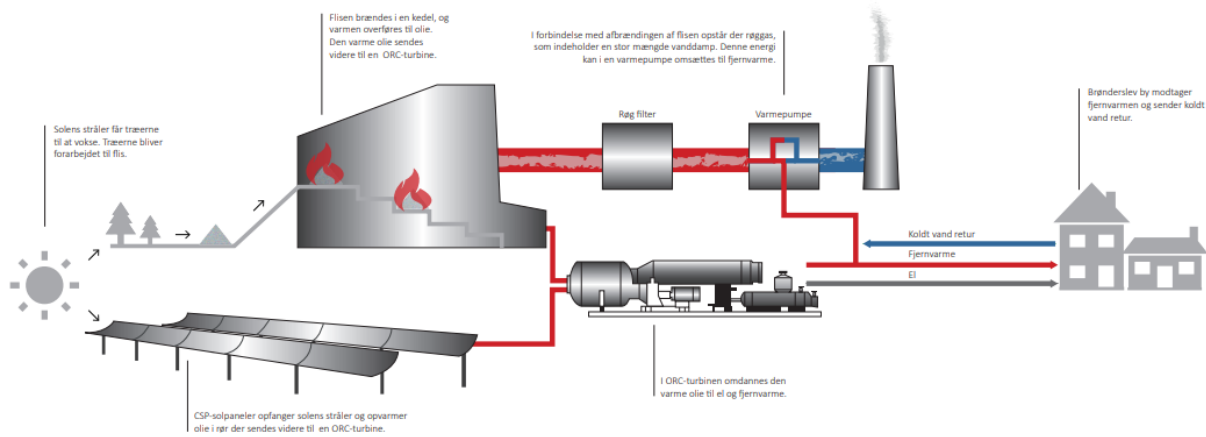


**Figure 1:** Simplified schematic of the Brønderslev CHP biomass-CSP power plant [1].

The hybrid solar-biomass power plant is able to deliver 90% of the town's district heating needs, whereas the remaining heat is supplied by the old power plant that was kept primarily for delivering heat during peak load hours. The Brønderslev district heating grid also utilizes waste heat from a local glass manufacturing plant, which is not considered in this investigation.

## 1.2 Solar collector field

The solar collector field has a peak thermal output of 16.6 MW and is made up of 40 parabolic trough collectors (PTC). The collectors were installed during Fall 2016 and the solar field was operational from January 2017. The solar field covers an area of 9 hectares and is placed adjacent to the new power plant in order to reduce piping distance.

The parabolic trough collectors were been manufactured by Aalborg CSP, who also delivered the control system for the solar field. Each collector has a length of 120 m and a total width of 5.77 m. The PTCs are single-axis tracking, along an axis 29.9° east of north. While a North-South orientation gives the highest annual energy yield, this was not possible due to the geometry of the available plot of land.

The heat transfer fluid is Therminol 66, which is a commercially available high-temperature thermal oil that is suitable for the temperatures in the system [2]. The same heat transfer fluid is used in the biomass boiler loop, hence the solar loop is directly coupled.



**Figure 2:** Left: Close up photo of the parabolic trough collector mirrors and receiver tube. Right: Aerial photo of the solar collector field and power plant in the background.

Depending on the available irradiation, the solar collector field can be set to ORC mode or district heating mode. In the ORC mode, high-temperature heat is required and the inlet and outlet temperature setpoints are 252 and 312°C, respectively. For the district heating mode, however, a much lower temperature is desirable to reduce the heat loss in the solar collector field.

**Table 1:** Main parameters for the solar collector field.

Parameter	Value
Max. power output	16.6 MW
Trough length	120 m
Number of troughs	40
Number of loops	10
Total aperture area	26 930 m <sup>2</sup>
Azimuth orientation	29.9°
Row spacing	15 m
Heat transfer fluid	Therminol66

Before the inauguration of the plant, the originally granted subsidy scheme was withdrawn and it was not allowed to deliver heat from the solar field to the ORC and generate electricity. For this reason, the solar field has only delivered heat directly to the district heating network through a heat exchanger. A new subsidy scheme was granted in 2020 making it possible to demonstrate the operation of the ORC with heat from the CSP field and the biomass boilers. There is therefore data for the joint heat delivery to the ORC from the CSP field and biomass boilers for four days during April-June of 2020.



## 2. Performance assessment

The performance assessment is divided into four sections. First, the overall system performance is presented in Section 2.1, focusing on the monthly and annual energy contributions of the different sources. The solar thermal performance is then investigated in greater detail in Section 2.2. Finally, the tracking accuracy of the parabolic trough collectors is elucidated in Section 2.3 and the soiling of the pyrheliometer is discussed in Section 2.4.

### 2.1 Overall system performance

A simplified schematic of the combined heat and power plant (without the solar collector field) is shown in Figure 1. The inlet and outlet water from the district heating grid enters in the right part of the figure and is heated in multiple steps before being returned to the district heating grid.

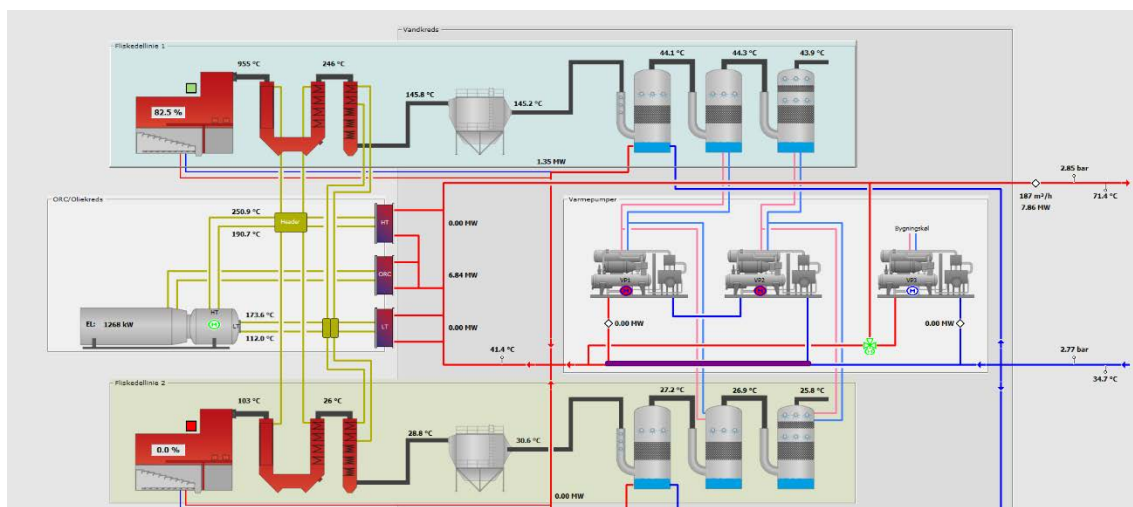


**Figure 3:** Simplified schematic of energy flows in the power plant.

When the district heating water enters the plant, it is first passed through the first flue gas scrubber, cooling the flue gas, after which part of the water is used to cool the biomass boiler grates. These two combined heat contributions are denoted "*Biomass boiler 1*" for the one biomass boiler and denoted "*Biomass boiler 2*" for the other. In parallel, part of the district heating water to the plant is heated by the three heat pumps. Next, the combined water flow is heated to the final outlet temperature in three subsequent heat exchangers (HX) denoted; Low temperature HX, ORC condenser, and High temperature HX. Originally the High temperature HX was placed before the Low temperature HX, which resulted in unstable operation and difficulties when starting the ORC. The order of the two heat exchangers was switched during 2020, resulting in a much smoother and faster starting of the ORC.

The annual energy contributions to the district heating output of the plant for each of the aforementioned sources are listed in Table 2. A more detailed overview on a monthly basis is shown in Figure 4. From the figure it is clear that the production profile of the biomass plant and the solar collector differ on a seasonal scale. The biomass plant only operates from September to June, whereas the solar collector field primarily generates heat from April to September.

**Table 2:** Annual contribution to the district heating network in MWh for each source.  
 \*Values for 2018 are from March and values for 2020 are only until October 15<sup>th</sup>.

	2018*	2019	2020*
Biomass boiler 1	5513	8836	5784
Biomass boiler 2	5496	7451	5556
High temperature HX	9989	4509	1062
Low temperature HX	709	396	132
ORC condenser	33077	52434	34792
Heat pumps	5143	6320	1064
Biomass plant total	61218	80756	48228
Solar collector field	11073	9793	11024
Electricity generation (gross)	5781	11325	8180
Electricity generation (net)	5745	11247	8134

Furthermore, from the values in the table, it is possible to estimate the annual efficiency of the ORC, by dividing the net electricity output by the heat output of the ORC condenser and the net electricity generation. For 2020 this results in an estimated efficiency of 19%.

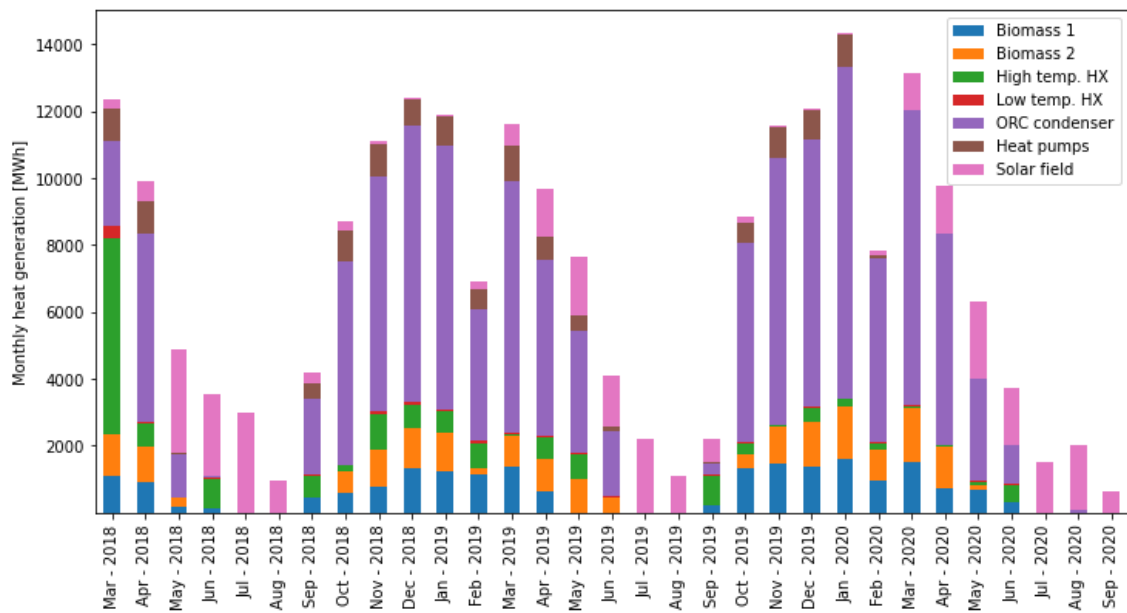


**Figure 4:** Monthly heat generation by source.

The efficiency of the ORC turbine depends largely on the power output level, which can be seen in the scatter plot in Figure 5. The plot shows the hourly efficiency of the ORC, calculated as the net power output divided by the thermal input. The maximum efficiency is approx. 22% when the turbine operates at full capacity, whereas at 40% part-load the efficiency is 15-18%.

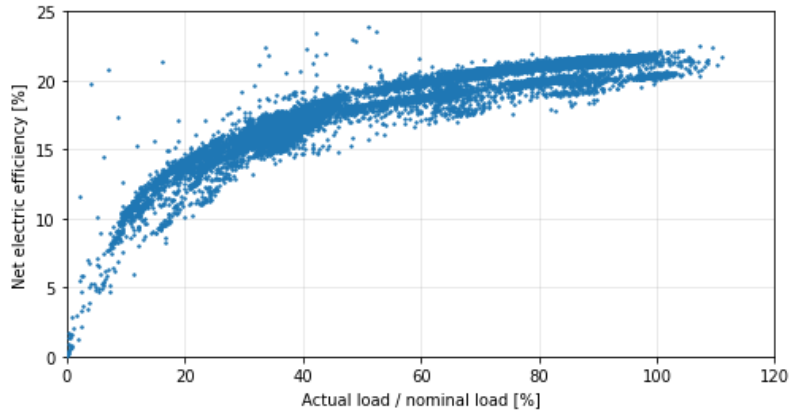


**Figure 5:** The net electric efficiency of the ORC vs. normalized power output.

The joint supply of hot thermal oil from the biomass boilers and the CSP field was demonstrated on May 5<sup>th</sup>, 2020. The heat and power generation during the day is shown in Figure 6, in addition to the temperature to and from the CSP field and the main valve statuses. The solar field starts producing heat around 6 am and gradually begins supplying heat to the ORC at 7 am. This is achieved by opening the valve between the ORC and CSP loops (MV292), which can be seen in the bottom subplot. Joint supply of heat from the CSP and biomass boilers was one of the milestones of the project and was successfully completed on April 22<sup>nd</sup>, May 5<sup>th</sup> and June 9<sup>th</sup> and 10<sup>th</sup>.

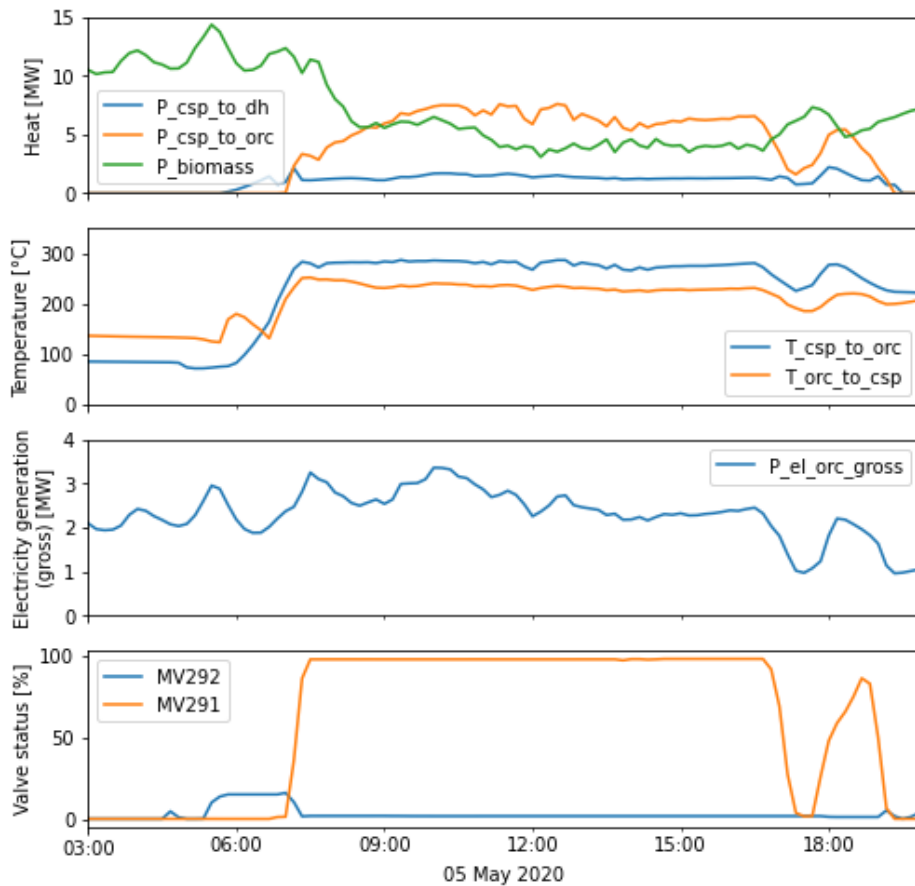


**Figure 6:** Measurements during thermal oil supply to the ORC.

## 2.2 Solar collector field thermal performance

The monthly in-plane direct irradiance and heat generation from the solar collector field for 2020 is shown in Figure 7. The DNI in-plane is the incident irradiance on the collector surface, meaning that it has been corrected for the incidence angle. The irradiance denoted DNI in-plane (tracking) is the DNI in-plane irradiance but only for the periods where the tracking was active. There are multiple reasons why the tracking is not always active, including maintenance, periods where the irradiance is below the set threshold of  $120 \text{ W/m}^2$ , etc. The heat output shows a strong seasonal behavior, with a maximum heat generation in May and practically no heat generation in January. Overall a strong correlation between the available solar resource and heat generation can be observed.

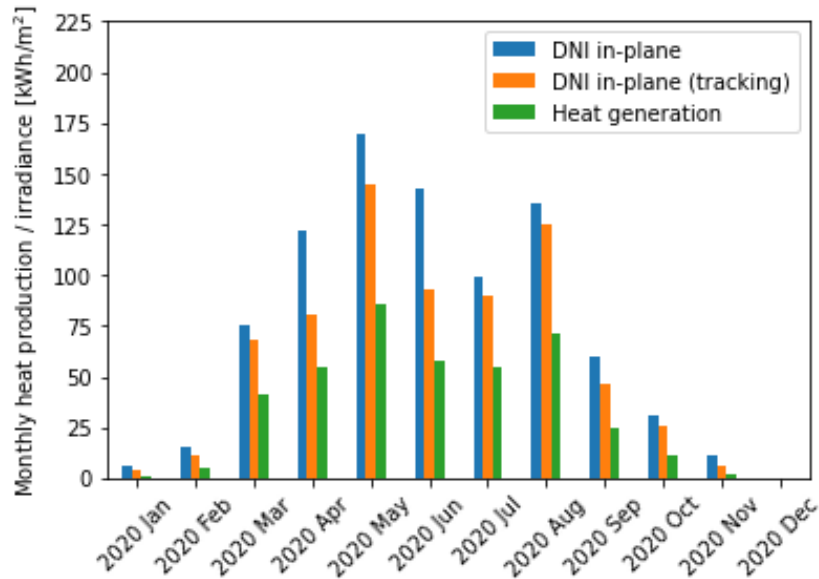


Figure 7: Monthly heat production and direct in-plane irradiance.

The correlation between the available solar resource and heat generation can be more clearly observed in Figure 8. The figure shows a very clear linear trend between the daily heat production and the daily direct irradiance in-plane.

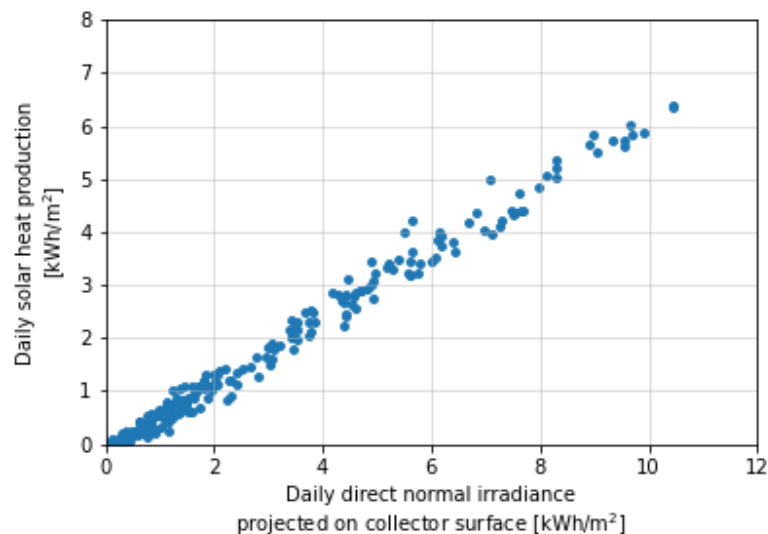
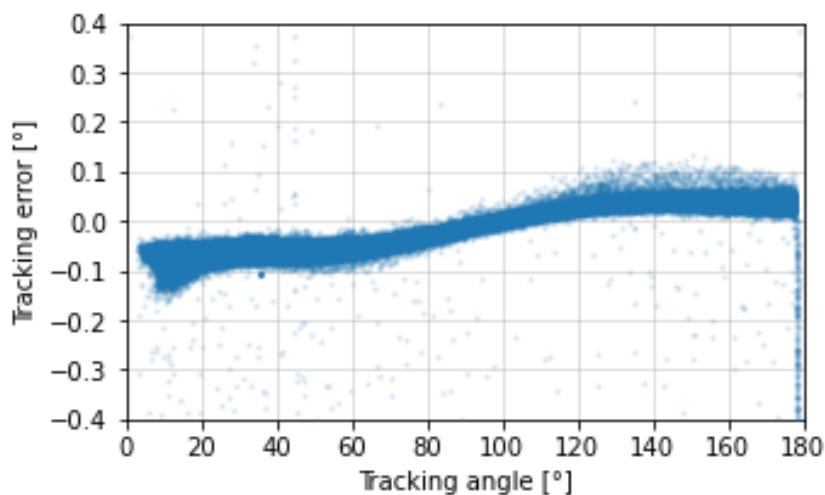


Figure 8: Comparison of the daily heat production vs. in-plane direct radiation for May-September 2020.

### 2.3 Tracking error test

Accurate tracking is essential for concentrating solar collectors, as even small tracking errors can reduce power output significantly. The effect of tracking error on Aalborg CSP's collectors installed in Tårs was investigated by Sallaberry in [3]. The study found that a tracking error of  $1^\circ$  can result in a power reduction between 50% and 80%, depending on the longitudinal incidence angle.

The tracking accuracy was assessed for all of the collectors at the Brønderslev solar collector field by comparing the measured tracking angle with the ideal tracking angle. The ideal tracking angle is that which minimizes the incidence angle on the collector and was calculated from the axis orientation and the instantaneous sun position. All of the collectors showed a similar distribution of tracking errors, an example of which is shown for one collector in Figure 9. The figure shows the tracking error vs. the tracking angle, where the tracking angle is the rotational angle around the tracking axis (at  $0^\circ$  the collector is vertical facing west, at  $90^\circ$  the collector is horizontal, and at  $180^\circ$  the collector is vertical facing east). The tracking error is defined as the measured tracking angle minus the ideal tracking angle.



**Figure 9:** Tracking error vs. tracking angle for one collector.

A clear relationship between the tracking error and the tracking angle can be observed in Figure 9, with negative errors when the collectors face east and positive errors when the collectors face west. This distribution of tracking errors is due to the gravitational torque on the troughs, which is in the opposite direction when the collector is on either side of the horizontal position. When the collector is in the horizontal position, there is no gravitationally induced torque, hence the tracking errors are practically zero. However, the tracking errors are generally below  $0.1^\circ$ , which according to [3] has a negligible impact on the power output.

The tracking error due to the gravitational torque on the troughs may have an increased effect with increasing distance away from the drive motor. This could be investigated in the future by placing an additional inclinometer or angular sensor at the end of the trough, where the largest tracking error is expected to occur. This is also recommended by IEC 62862 for tracker error testing, which specifies a minimum requirement of two angular sensors.

Furthermore, the effects of wind loading had on tracking accuracy were investigated. This was done by calculating the 95<sup>th</sup> percentile of the tracking accuracy within each bin of wind speed (every 1 m/s). No noticeable trend of the tracking accuracy with respect to the wind speed was found.

## 2.4 Direct radiation sensor soiling

Measurement of direct solar radiation for concentrated solar collector fields is essential for optimum operation and accurate performance assessments. The reason that direct solar radiation is particularly important to concentrating collectors such as parabolic trough collectors, is that only the direct radiation can be concentrated and utilized to generate energy. Direct solar radiation, also known as beam radiation, can be measured with a pyrheliometer. Modern pyrheliometers generally have a 5° opening and need to be mounted on a two-axis solar tracker to be aligned with the sun as it moves during the day.

At the Brønderslev solar field, direct irradiance is measured with an EKO MS-56 pyrheliometer mounted on an EKO STR-21G solar tracker as shown in the photo to the left in Figure 10. The solar tracker is mounted at the top of a mast that is taller than the parabolic trough collectors. This ensures that the pyrheliometer is never shaded throughout the day, but the downside is that it makes regular cleaning difficult. Therefore, as an effort to prevent dirt from accumulating on the pyrheliometer, a BlackPhoton Airshield was mounted on the pyrheliometer. The Airshield continuously blows air across the surface of the pyrheliometer, with the intention of acting as a barrier to keep dust and dirt from settling on the sensor glass.

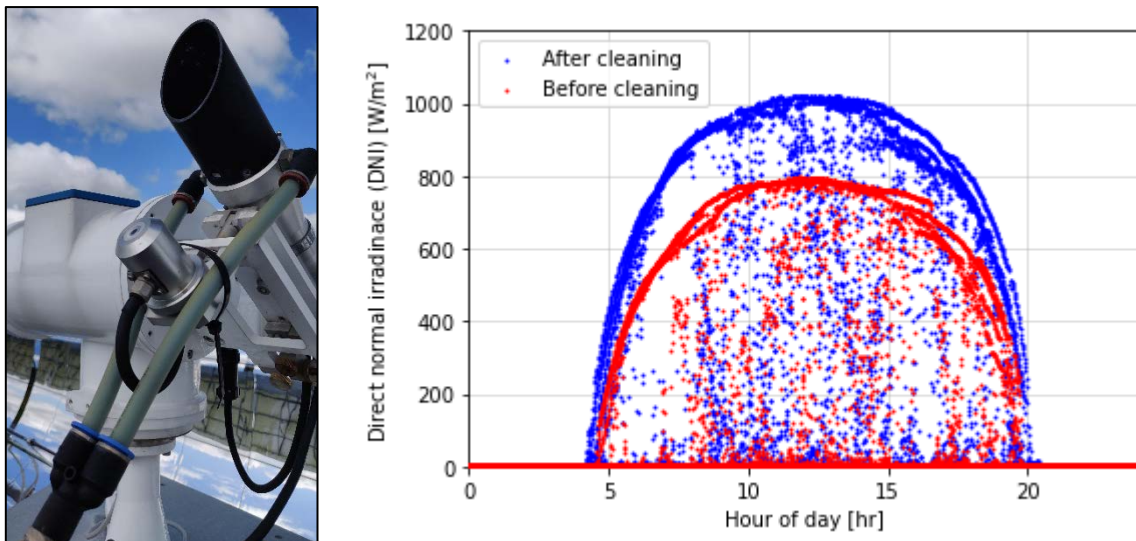


**Figure 10:** Left: photo of the pyrheliometer with the Airshield (black cover) and two-axis sun tracker. Right: Scatter plot of the direct irradiance measurements seven days before and after cleaning on May 6<sup>th</sup>, 2020.

However, the Airshield was found to not be very effective in keeping the pyrheliometer clean. This is clearly shown in the scatter plot in Figure 10, which shows that the sensor underestimated the direct irradiance by 22% prior to being cleaned. In fact, the Airshield most likely even contributed to increased soiling of the sensor, as there was no way for rain to wash clean the sensor. Poor irradiance measurements pose a serious limitation to the investigations of the solar collector field performance, as it is impossible to do long-term studies, e.g., characterize the soiling of the mirrors and receiver tubes, seasonal trends of the efficiency.

### 3. Solar Field Performance Characterization

In this section, the performance of the solar collector field is characterized using the quasi-dynamic test (QDT) method. With the adoption of the international standard IEC 62862-3-2: 2018 – *General requirements and test methods for large-size parabolic-trough collectors* [4], this method has become the recommended method for characterizing parabolic-trough collectors. The standard builds largely on the methodology of ISO 9806:2017 [5] but extends this by making it possible to take into account reflection measurements to allow for the consideration of soiling.

The method is only applicable for outdoor testing and is generally performed on a single collector. However, for the case of the Brønderslev solar collector field, the flow rate is only accurately measured on the return pipe from the entire solar collector field. Hence, it is only possible to characterize the solar collector field, including the supply and return piping, and not an individual collector.

The QDT method accounts separately for heat gains from the direct and diffuse irradiances and can be performed during non-steady-state conditions, hence it can be applied to outdoor in-situ measurements. The QDT method describes the power output of essentially any solar thermal collector using the following equation:

$$\frac{\dot{Q}}{A} = \left[ \eta_{0,b} K_b(\theta_L, \theta_T) G_b + \eta_{0,b} K_d G_d - a_1(\vartheta_m - \vartheta_a) - a_2(\vartheta_m - \vartheta_a)^2 - a_3 u(\vartheta_m - \vartheta_a) \right] + a_4(E_L - \sigma T_a^4) - a_5(d\vartheta_m/dt) - a_6 u G - a_7 u (E_L - \sigma T_a^4) - a_8(\vartheta_m - \vartheta_a)^4 \quad \text{Eq. 1}$$

where the two first terms are heat gains from the direct and diffuse irradiance, respectively, and the remaining terms are loss terms.  $A$  is the collector aperture area, which is commonly used for parabolic trough collectors, whereas when reporting results for flat plate collectors the gross area is used.

The collector coefficients, which depend on the type of collector and its design, can be used to predict the power output for any given set of operating conditions. Determining these coefficients is the core of the QDT method and is done by fitting Eq. 1 to representative measurement data.

According to ISO 9806:2017, the parameters  $a_2$ ,  $a_3$ ,  $a_4$ ,  $a_6$ ,  $a_7$ , and  $K_d$  may be set to zero for collectors with a concentration ratio greater than 20, which includes practically all parabolic trough collectors.

For one-axis tracking collectors, the incidence angle modifier  $K_b(\theta_L, \theta_T)$  simplifies to  $K_b(\theta_L)$ , since the transversal incidence angle is zero.  $K_b(\theta_L)$  is modeled using the equation proposed in [6] and recommended by IEC 62862-3-2 for parabolic trough collectors:

$$K_b(\theta_L) = 1 - \frac{b_1 \cdot \theta_L + b_2 \cdot \theta_L^2}{\cos(\theta_L)} \quad \text{Eq. 2}$$

Generally, tests are performed under relatively constant operating conditions (flow rate and mean temperature), however, this option is limited when it comes to an actual plant. The inability to manipulate operating conditions gives rise to certain limitations, e.g., the temperature range of measurement data is relatively limited, even though it is recommended to have measurements

covering the entire operating temperature range. The reason for this is that with greater variation in the data, the different parameters are more easily determined by the QDT method and the uncertainty of the parameters is reduced. One disadvantage of making tests of an entire solar collector field is the large residence time, e.g., the time it takes the fluid to enter, run through, and return from the collector field. Additionally, the time delay of each collector loop is different, as the pipe lengths differ significantly. Therefore, to average out these effects, the QDT was performed on data resampled with a frequency of 30 minutes.

Perhaps the most important step in the QDT method is the selection of representative and accurate data for the parameter regression. It is especially important to ensure that the data includes sufficient variability. For example, it is important to include days with drifting clouds in order to determine the thermal capacity of the system and it is important to cover a large temperature range to determine the heat loss coefficients.

For the selection of input data for the QDT method, only days where the pyrheliometer has been cleaned within the past week are considered. As mentioned in Section 2.4 the cleaning of the pyrheliometer was infrequent, however, an extra effort was made during 2020 where the pyrheliometer was cleaned six times during the period from May to September. Also, only days where there is solar heat production were included. The resulting data set consists of 14 days between May and September 2020.

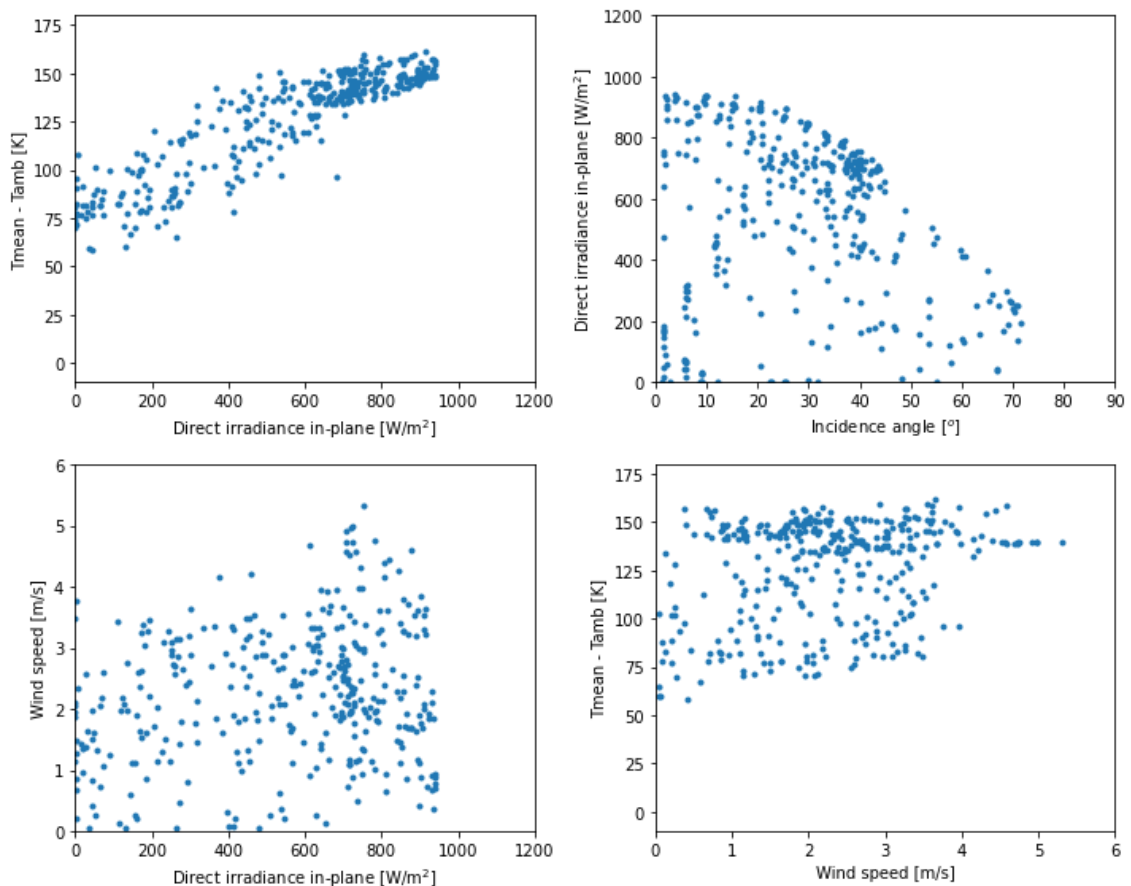


**Figure 11:** Scatter plots for comparing the variability of the selected and resampled measurement data.



The variability of the selected measurement data can be assessed from Figure 11. The subplot in the top left compares the temperature difference between the mean collector fluid and the ambient (the driving force behind the heat losses) to the direct in-plane irradiance. A trend of increasing temperature with increasing irradiance can be observed. Under ideal conditions, there would not be any detectable trend and the measurement data would cover a greater range of operating temperatures. In the subplot in the top right, the direct in-plane irradiance is plotted against the incidence angle. This plot shows a relatively random distribution, hence it is expected that the incidence angle modifier can be more accurately determined. Since there is only data for incidence angles up to approx. 70°, the prediction range is also only valid in this interval.

The significant collector parameters and their values from the least-squares regression are listed in Table 3. The table also includes the standard deviation and t-score for each parameter, which is used to assess the confidence of the value. Parameters  $a_2$ ,  $a_8$  and  $b_2$  were initially included in the model, however, the t-score for each of them was below 3, and hence they were omitted according to ISO 9806.

Table 3: Solar collector coefficients for Brønderslev solar collector field derived using the quasi-dynamic test method.

Parameter	Collector field	Std. deviation	T-score	Unit
$\eta_0$	72.7%	0.6%	113	-
$a_1$	0.271	0.032	8.5	W/(m <sup>2</sup> K)
$a_5$	6721	146	46	J/(m <sup>2</sup> K)
$b_1$	$2.6 \cdot 10^{-3}$	$0.1 \cdot 10^{-3}$	25	-

It is important to note that the collector coefficients in Table 3 correspond to the entire collector field, including the approx. 1200 m of piping connecting the solar collector loops to the power plant. Therefore, the heat loss term ( $a_1$ ) and the heat capacity ( $a_5$ ) are representative of the solar collector field and not only the solar collectors. Specifically, this means that heat loss coefficient  $a_1$  includes the heat losses from the pipes and effective thermal capacity  $a_5$  includes the additional thermal capacity of the fluid in the pipes and the piping itself.

The contribution of the pipes to the heat loss term ( $a_1$ ) is, however, expected to be relatively low. To put this in perspective, the theoretical heat loss from the pipes can be calculated from the piping dimensions and the thermal conductivity of the insulation (0.053 W/(m K)) and steel (57.5 W/(m K)). The influence of the heat transfer convective coefficients from the liquid to the pipe and from the outer pipe surface to the air are neglected due to their insignificant influence. The theoretical heat loss from the pipes can then be calculated to be 467 W/K or 0.017 W/(m<sup>2</sup> K) relative to the collector aperture area. The heat loss from the evacuated receiver tube itself is between 0.04 and 0.10 W/(m<sup>2</sup> K) for a receiver absorber temperature of 154°C and 346°C, respectively [7]. It should be noted that these measured heat loss values are in reference to the absorber temperature, which is higher than the fluid temperature, as heat is transferred from the absorber to the fluid. These measurements only considered the heat loss from the evacuated tube itself, and not the connections, from which a significant heat loss likely occurs. The large difference in the specific heat loss at 154°C and 346° signifies that the heat loss coefficient is

temperature dependent even though neither  $a_2$  nor  $a_8$  were found to be significant. This is likely due to the measurement data not having a large enough temperature range.

The thermal capacity, on the other hand, was significantly greater for the solar collector field compared to just the solar collectors. This is due to the solar collectors themselves only containing a relatively small amount of liquid (approx. 2 m<sup>3</sup> per loop) relative to the entire system including the piping and collectors (72 m<sup>3</sup>). To verify the thermal capacity derived using the QDT method in Table 3, the thermal capacity of the solar field can be estimated based on the ‘calculation method’ described in section 25 of ISO-9806. This method relies on calculating the effective thermal capacity from the sum of the thermal capacities of the individual collector elements. Elements that are not in direct contact with the fluid are multiplied by a weighting factor lower than 1. The weighting factor for the thermal capacity of the liquid and pipes is 1, which by far are the largest contributors to the thermal capacity. Thus, the thermal capacity will be calculated as the sum of only the contributions of these two elements.

The total amount of heat transfer fluid in the system is 72.3 m<sup>3</sup> of Therminol66, which has a specific heat capacity of 2122 J/(kg K) and a density of 890 kg/m<sup>3</sup> at 180°C. The thermal capacity of the liquid can then be calculated as the product of the volume, specific heat capacity, and density, which, when divided by the aperture area, is 5070 J/(m<sup>2</sup> K). Similarly, the thermal capacity contribution of the pipes is 1156 J/(m<sup>2</sup> K), based on a steel volume of 8.6 m<sup>3</sup> for all the pipes, a specific heat capacity of 461 J/(kg K), and a density of 7850 kg/m<sup>3</sup>. Combining the contribution from the liquid and the steel, the estimated effective thermal capacity is 6226 J/(m<sup>2</sup> K). This value is only slightly lower than what was determined from the QDT method in Table 3 and confirms the results found with the QDT method.

The value for the linear incidence angle modifier coefficient,  $b_1$ , is also given in Table 3. The second-order term was found to have a t-score less than 3 and was therefore removed (i.e., is set to zero in Eq. 2). In Figure 12 the incidence angle modifier from Eq. 2 is compared to the ASHRAE method which has previously been used for Aalborg CSPs collector [8]. The new method (Valenzuela) shows a lower value for the incidence angle modifier for angles between 5° and 70°, which has a direct impact on the predicted power output.

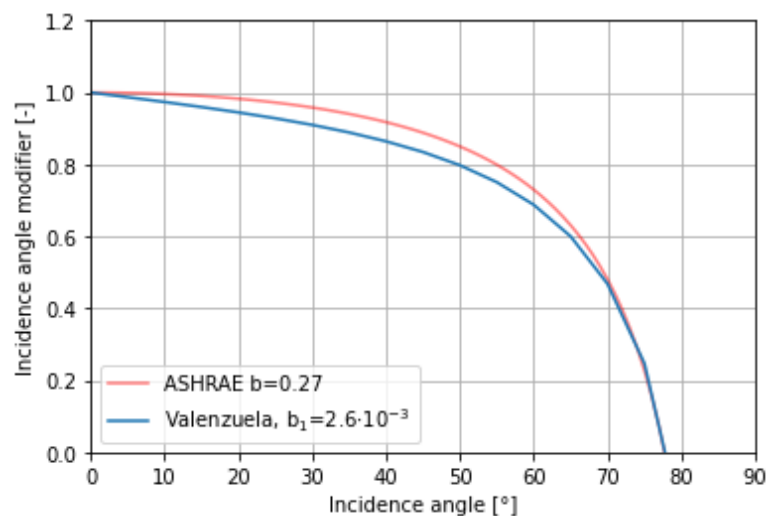


Figure 12: Incidence angle modifier vs. incidence angle.

The collector coefficients determined from the QDT method in Table 3 are compared to values for similar parabolic trough collectors in Table 4. One of the studies listed in the table is the pilot study [8] from 2015, where two 120 m collectors were tested in Brønderslev. The study used an optical efficiency of 75%, which compared well with the obtained measurements. While the optical efficiency determined from the QDT method (72.7%) is slightly lower, this is not surprising, as it is inevitable that the mirrors and receiver tubes experience some soiling during four years of operation without being cleaned. The uncertainty of the optical efficiency should also be considered when comparing values. The generally accepted uncertainty of the optical efficiency determined from QDT is around  $\pm 1\%$  among accredited test institutes, which has been determined from an extensive round-robin test.

The collector coefficients for Tårs were also determined using the QDT method, though the heat loss coefficient was estimated from the datasheet of the evacuated receivers and not experimentally determined. The thermal capacity is much lower for the Tårs study, which is because the length of the pipes there was much shorter than in Brønderslev. The EUROtrough is a parabolic trough collector very similar to Aalborg CSP's. When comparing the heat loss coefficient to the EUROtrough, it is necessary to also consider the  $a_8$  term. E.g. at a delta temperature of 200 K, the heat effective heat loss for the EUROtrough is 0.858 W/(m<sup>2</sup> K), which is significantly higher than Aalborg CSPs collector.

**Table 4:** Comparison of collector coefficients for different parabolic trough collectors.  
\*The heat loss value for Tårs was only theoretically determined.

Parameter	Brønderslev	Pilot plant [8]	Tårs [9]	EUROtrough [10]	Unit
$\eta_0$	72.7%	75.0%	73.6%	72.2%	-
$a_1$	0.271	0.06	0.04*	0.192	W/(m <sup>2</sup> K)
$a_5$	6721		2962	1749	J/(m <sup>2</sup> K <sup>2</sup> )
$a_8$	-		-	$8.33 \cdot 10^{-8}$	W/(m <sup>2</sup> K <sup>4</sup> )

## 4. Simulation model

This section presents a TRNSYS simulation model of the solar collector field. The model and the control strategy are described in Section 4.1 and the model validation is presented in Section 4.2. Finally, the model is used to investigate the impact of row spacing and the axis azimuth on the thermal performance in Section 4.3.

### 4.1 Model description

A simulation model of the Brønderslev CSP field was developed in the simulation software TRNSYS [11]. Other simulation software that were considered includes NREL's System Advisor Model (SAM) [12], Dymola, and the Carnot toolbox in MATLAB. However, TRNSYS was chosen due to its large number of validated thermal components and its well-documented performance for simulating solar thermal district heating systems (see [13]–[15] among others).

A schematic of the simulation model is shown in Figure 13, with the solar collector loop to the left (primary side) and the district heating network to the right (secondary side). The major system components are listed in Table 1.

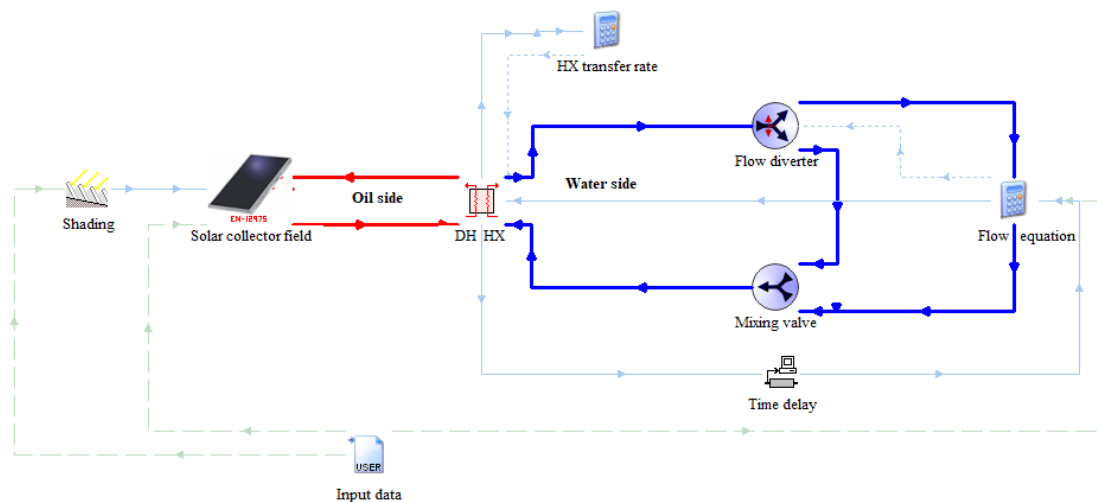


**Figure 13:** Schematic of the TRNSYS simulation model.

The solar collector field is simulated using the TRNSYS component Type 1289 from TESS. The model is based on Eq. 1, though it does not include the  $a_7$  and  $a_8$  terms. The reason for choosing Type 1289 over other similar modes, e.g., Type 1288 and 1290, is that 1289 reads the incidence angle modifier from a one-dimensional table. This table was generated for every  $5^\circ$  and the incidence angle modifier was calculated according to Eq. 2. The collector coefficients in Table 3 were given as input parameters. In addition, the direct irradiance on the collector surface from Type 30b was given as input, as was the ambient temperature, incidence angle, and wind speed from the input file.

Inter-row shading is implemented with the shading component Type 30b, which calculates the shading fraction and shaded beam radiation for single-axis tracking parabolic trough collector fields [16]. Heat is exchanged between the primary and secondary sides in a parallel flow heat

exchanger, which is simulated using the parallel flow heat exchanger, Type 5a. The heat exchanger capacity,  $k$ , is modeled using the empirical relationship:

$$k = k_{nom} \cdot \left( \frac{\dot{m}_{csp}}{\dot{m}_{csp,nom}} \right)^{0.45} \cdot \left( \frac{\dot{m}_{dh}}{\dot{m}_{dh,nom}} \right)^{0.45} \quad \text{Eq. 3}$$

where  $k_{nom}$  is the nominal heat exchanger capacity (1098 W/(m<sup>2</sup> K)), and  $\dot{m}_{csp}$  and  $\dot{m}_{dh}$  are the mass flow rate on the primary and secondary sides, respectively. The subscript *nom* refers to the nominal values, where  $\dot{m}_{csp,nom} = 98.8$  kg/s and  $\dot{m}_{dh,nom} = 57.3$  kg/s. The heat exchanger area is 123 m<sup>2</sup>.

**Table 5:** System component and TRNSYS type numbers.

System component	Component name	Type
Solar collector field	Generic Solar Collector Model Using the EN12975-2 Efficiency Approach - 1D IAMs	1289
Shading	Collector Array Shading: Parabolic Trough	30b
Heat exchanger	Heat exchanger - parallel flow	5a
Flow diverter	Controlled flow diverter	11f
Tee piece	Tee piece	11h
Time lag	Time lag data	93
Input data (validation)	Data Reader For Generic Data Files	9e
Input data (annual simulation)	Weather data processor – TMY2	15-2

#### 4.1.1 Control strategy

In order to avoid overheating, a minimum flow rate through the solar collectors and on the secondary side of the heat exchanger is required. Furthermore, to be able to control the outlet temperature to the district heating network, a bypass loop is implemented on the secondary side, as shown in Figure 13. This allows for the district heating water to be recirculated until the outlet temperature from the heat exchanger matches the setpoint. As the power transferred in the heat exchanger increases, the flow diverter will increasingly redirect flow to the district heating grid until there is no longer any recirculation and the flow in the bypass loop is zero. Once this stage is reached, only the flow rate is regulated in response to changes in the transferred heat to realize the setpoint temperature.

The flow rate through the heat exchanger on the primary side,  $\dot{m}_{dh,hx}$ , which will result in an outlet temperature equal to the setpoint, can be calculated as based on the theory of a feed-forward controller:

$$\dot{m}_{dh,hx} = \begin{cases} \max\left(\frac{\dot{Q}_{hx}^{i-1}}{(T_{dh,out,set} - T_{dh,in}) cp_{water}}, \dot{m}_{dh,min}\right), & \dot{m}_{csp} > 0 \\ 0, & \dot{m}_{csp} = 0 \end{cases} \quad \text{Eq. 4}$$

where  $\dot{Q}_{hx}^{i-1}$  is the heat transferred through the heat exchanger in the previous time step,  $\dot{m}_{dh,min}$  is the minimum flow rate on the secondary side of the heat exchanger (42 kg/s).  $T_{dh,out,set}$  is the desired set point of the temperature to the district heating grid,  $T_{dh,in}$  is the temperature of the water from the district heating grid, and  $cp_{water}$  is the specific heat capacity of water. The flow rate is equal to zero when the flow rate on the secondary side is equal to zero ( $\dot{m}_{csp} = 0$ ).

Since the water side of the heat exchanger is simulated without any heat capacity, any heat transferred through the heat exchanger needs to be transferred to the district heating grid. During periods where  $\dot{m}_{dh} = \dot{m}_{dh,min}$ , a fraction of the flow is recirculated as previously mentioned. The fraction of the water through the heat exchanger which is recirculated ( $f_{recirculation}$ ) can be calculated based on the fact that all of the heat transfer through the heat exchanger needs to be delivered to the district heating grid:

$$f_{recirculation} = 1 - \min\left(\frac{\dot{Q}_{hx}}{\dot{m}_{dh,min} (T_{dh,out,set} - T_{dh,in}) cp_{water}}, 1\right) \quad \text{Eq. 5}$$

The mass flow rate of water that is sent to the grid can then be calculated from the recirculation fraction as:

$$\dot{m}_{dh,net} = \dot{m}_{dh,hx} \cdot (1 - f_{recirculation}) \quad \text{Eq. 6}$$

Similarly, the flow rate through the solar collector field (primary side) is calculated as:

$$\dot{m}_{csp} = \begin{cases} \min\left(\max\left(\frac{\dot{Q}}{(T_{csp,out,set} - T_{csp,in}) cp_{oil}}, \dot{m}_{csp,min}\right), \dot{m}_{csp,max}\right), & DNI \geq 50 \frac{W}{m^2} \\ 0, & \text{otherwise} \end{cases} \quad \text{Eq. 7}$$

where  $\dot{Q}$  is the power output of the solar field calculated according to Eq. 1,  $T_{csp,out,set}$  is the solar collector field outlet set point temperature,  $T_{csp,in}$  is the inlet temperature to the solar collector field, and  $cp_{oil}$  is the specific thermal capacity of the heat transfer fluid.  $\dot{m}_{csp,min} = 70$  kg/s and  $\dot{m}_{csp,max} = 118$  kg/s are the lower and upper threshold limits, respectively, for the flow rate in the solar collector loop. The lower limit is imposed to avoid overheating in the solar collector field, whereas the upper limit corresponds to the maximum flow rate the pump can deliver.

## 4.2 Model validation

To verify that the model performs as expected, given its assumptions and potential limitations, it is necessary to validate the model. The model is validated by simulating a period where the boundary conditions are fixed and comparing the results with measurement data.

The specified model inputs are the measured weather parameters (direct radiation, wind speed, and air temperature), mass flow rate on the primary side, and the inlet district heating temperature. Also, the setpoint for the district heating temperature is set to 88°C.

The validation period was from May 5<sup>th</sup> to October 31<sup>st</sup>, 2020, as this was the period where the pyrheliometer was most frequently cleaned (five times during the period).

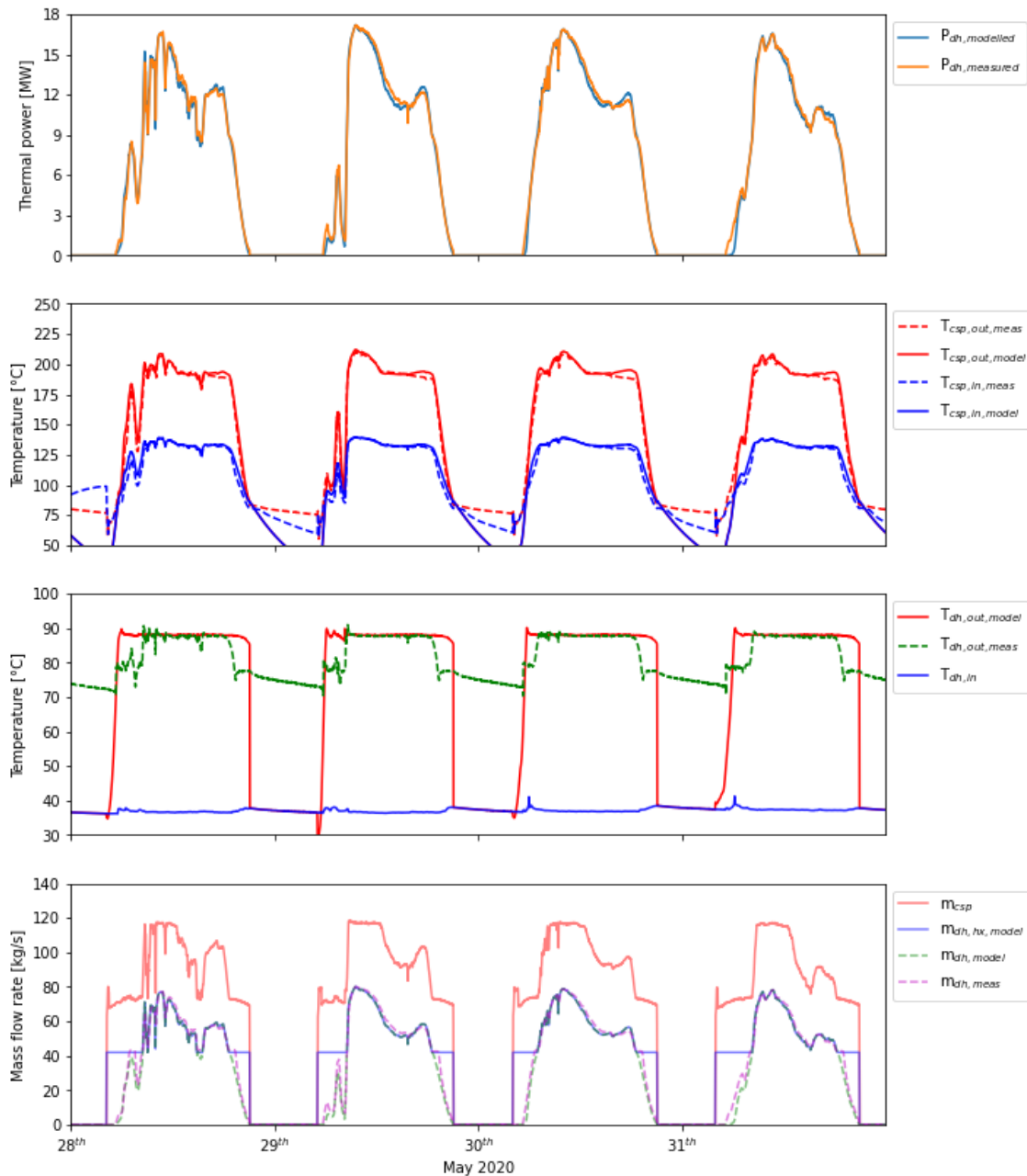


**Figure 14:** Comparison of measured and simulated values during four days of the validation period.

The simulation results and measured data for four days of the validation period are shown in Figure 14. In the top subplot of the figure, the measured and simulated heat transferred to the district heating grid are compared. Both for the first day, which had some drifting clouds, and the rest of the days, which were practically cloudless, there was very good agreement between the measured and simulated power. Hence, the collector parameters determined in Section 3 seem to capture the collector field performance well. It should be noted that the pyrheliometer was cleaned on May 25<sup>th</sup>, so DNI measurements for the period in Figure 14 are considered accurate.

The second plot in Figure 14 shows the measured and simulated temperatures in and out of the collector field. There was also very good agreement between these. The temperature peaks that take place before noon occur because the maximum flow rate in the solar collector field is reached and, therefore, the temperature increases. The bottom subplot shows that the maximum flow rate was, indeed, reached. Whereas the primary flow rate was used as an input to the model, the flow rate in the secondary sides was calculated using the control strategy described in the previous section. Again, there seems to be very good agreement between the measured and simulated values, and the control strategy is even able to accurately capture the recirculation in the bypass loop.

In Figure 15, the simulated and measured hourly heat generation during the validation period is shown. The plot shows some scatter, but generally, there does not seem to be any bias in the prediction of the power output.

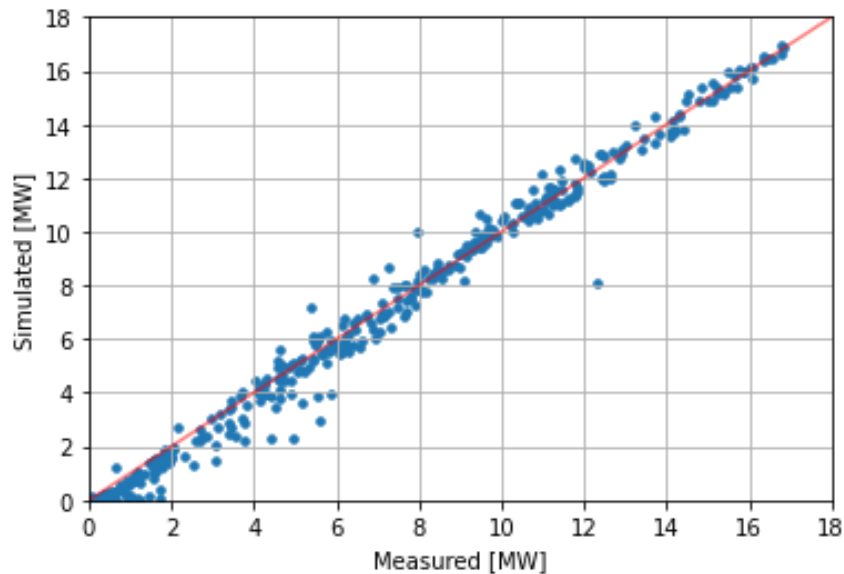


**Figure 15:** Comparison of simulated and modeled hourly heat output. Only days from May to October 2020 for which the pyrheliometer had been cleaned within the past 10 days are included.

Furthermore, the weekly energy generation for the entire validation period is shown in Figure 16. At first, it seems that there is a general tendency for the model to underestimate the heat production. However, for many of the weeks, the pyrheliometer was not cleaned. This results in an underestimation of the solar resource and, consequently, also the modeled output. However, for all weeks the difference between weekly measured and modeled energy production was between 0 and 3%.



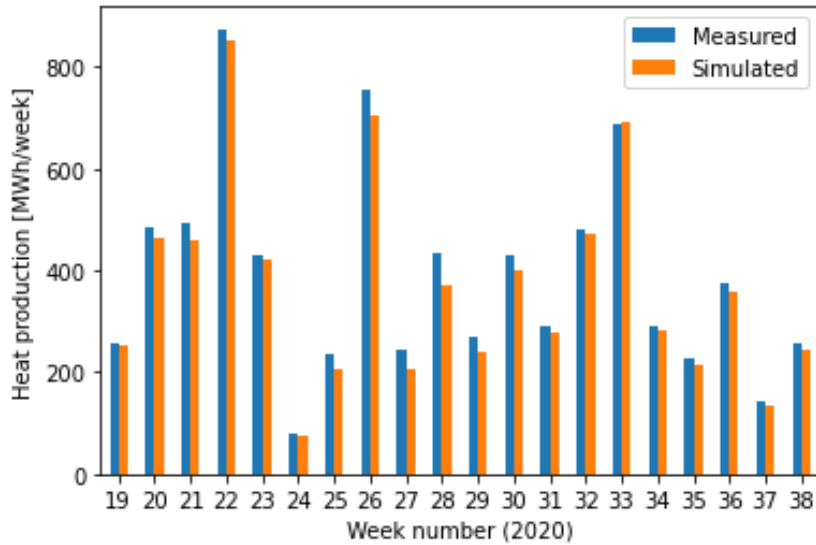


**Figure 16:** Weekly heat production, simulated and measured.

To illustrate the effect of soiling of the pyrheliometer, the ratio between the measured and simulated daily heat generation is plotted in Figure 17. During March and April, the pyrheliometer is never cleaned, and thus the soiling increases. This is the reason why the ratio increases during this period, as the simulated power decreases with increasing soiling. Immediately after May 6<sup>th</sup>, when the pyrheliometer was cleaned, the ratio drops to about one and remains so for the remainder of the period. Around the end of April, the modeled under-predicted the power output by 20%, clearly illustrating the importance and implications of a soiled pyrheliometer.

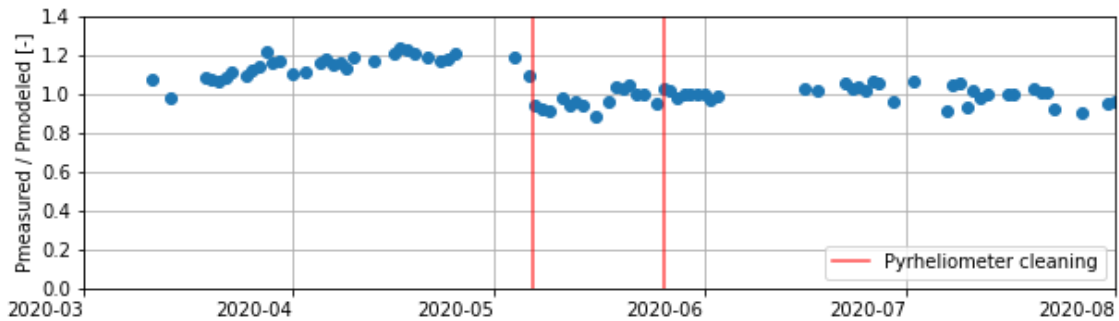


**Figure 17:** Plot of the ratio between measured and simulated daily heat generation.

### 4.3 Impact of row distance and axis orientation

The row distance and axis orientation are two defining parameters of any solar collector field that both have a large effect on the thermal performance. The parameters are often selected such that the levelized cost of heat is minimized within the specified constraints. With increasing row distance, shading is reduced and thermal performance is increased, however, these improvements come at the expense of increased land costs. Row spacing is often directly proportional to the land cost, e.g., if the row spacing is doubled, the required land (and land expenses) are also doubled. The selection of the tracking axis orientation is often more practical, with the aim of utilizing the available land area (restricted by its shape) as efficiently as possible without excessively compromising the thermal performance. This was also the case for the solar collector field in Brønderslev, which is oriented 29.9° east of north, to match the orientation of the available plot of land.

To determine the optimum configuration, it is necessary to understand the impact of each parameter. This section, therefore, presents simulated results of the annual and monthly thermal output for different row spacing and axis azimuth orientations for a solar collector field. With the exception of these two parameters, the solar collector field simulated has the same specifications as the solar field in Brønderslev, previously described in Section 4.1.

The annual heat generation has been simulated for row spacings between 7.5 and 27.5 m for every 2.5 m and axis azimuth orientations between 0° and 180° for every 10°. The reason for choosing 0°-180° is that this covers the entire range of possible orientations, as orientations 180° apart represent the same conditions. E.g., a solar field with an axis azimuth at 30° east of north is the same as one with an azimuth at 210° east of north for 1-axis tracking collectors. The annual heat generation for all combinations of row spacings and axis azimuth orientations are shown in Figure 18.

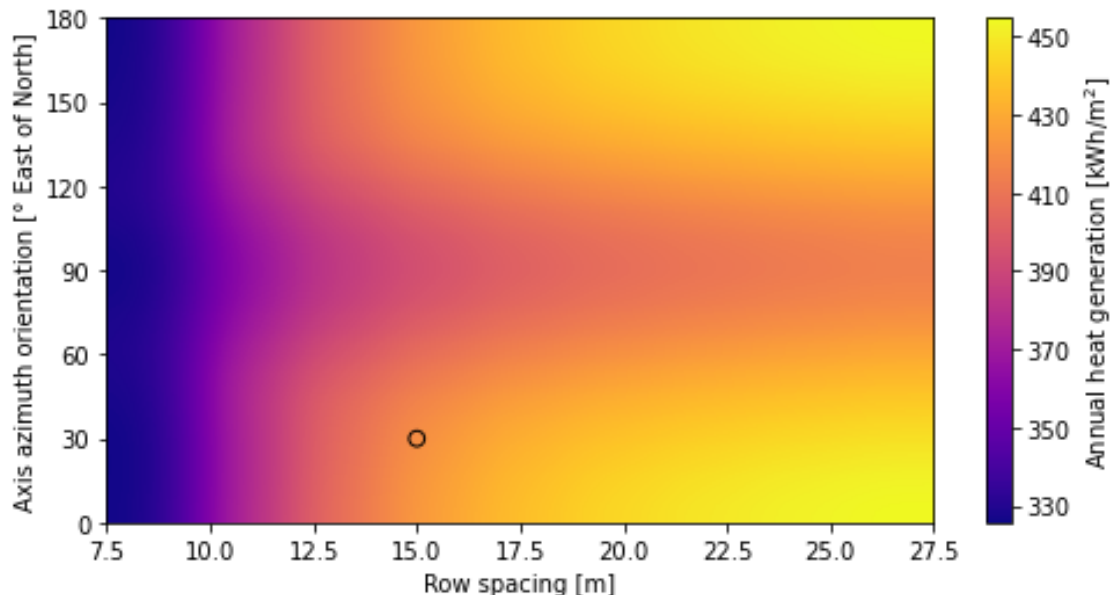


**Figure 18:** Annual heat production for different row spacings and axis azimuth orientations. The black circle represents the parameters for the collector field in Brønderslev.

Figure 18 shows a clear trend: For any axis azimuth, the annual heat generation increases with increasing row spacing. The increase in thermal performance is due to the reduced shading of

the collectors in the morning and afternoon. An increase in row spacing can result in a significant performance increase for short row spacings, though the benefit decreases with increasing row spacing and is essentially negligible for row spacings greater than 20 m.

To investigate the impact of row spacing in more detail, the monthly heat production for four different collector distances is shown in Figure 19. In addition to the monthly values, the annual heat generation is given in the legend box. For the base case (15m row spacing), the annual performance is 422 kWh/m<sup>2</sup>, which is reduced by 44 kWh/m<sup>2</sup> if the row spacing is reduced by 5 m and only increased by 15 kWh/m<sup>2</sup> if the row spacing is increased by 5 m. This trend can also be seen in the graph itself, as the difference in heat production between the 10 m and 15 m spacings is much greater than the difference between the 15 m and 20 m or between the 20 m and 25 m row spacing.

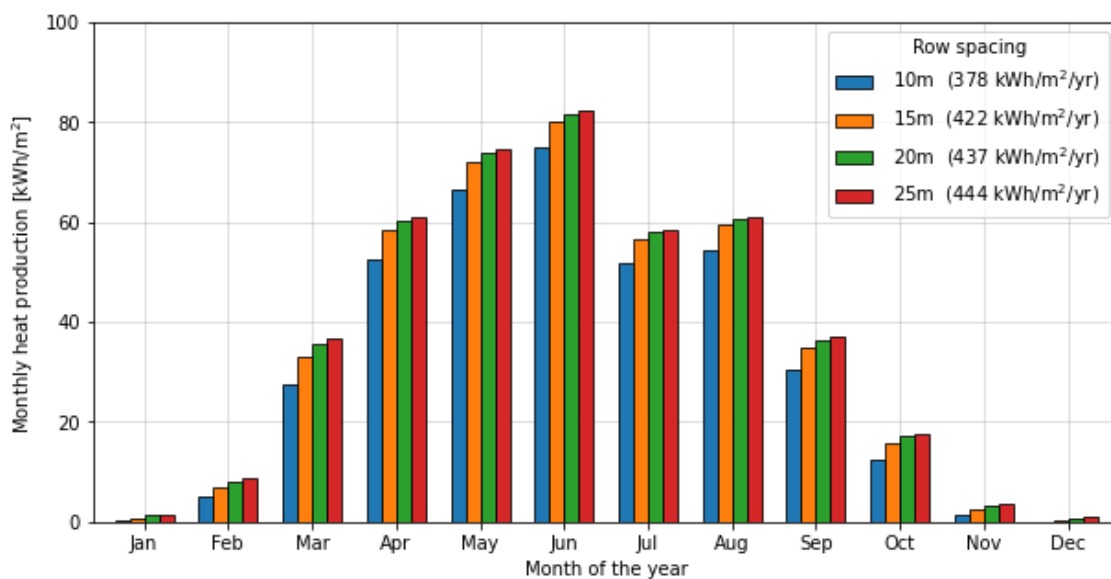


**Figure 19:** Monthly heat production for different row spacings. Axis azimuth = 30°.

Next, the monthly heat production for different axis azimuth orientations is presented in Figure 20. Figure 18 shows that the maximum thermal performance was achieved for an axis azimuth of 0° or 180°, a phenomenon that is also commonly reported in literature. While a North-South oriented tracking axis results in the greatest annual performance, Figure 20 shows that it does not result in the greatest heat generation for every month of the year. The North-South tracking axis orientation is favorable in months where the sun altitude is generally high, i.e., May through August, and the solar irradiation is the greatest. From October to March, an axis azimuth of 90° (East-West tracking axis) results in the greatest thermal performance. The reason for this is that the East-West tracking axis is significantly better at reducing the incidence angle when the sun is close to the south and has a low elevation, which are the general conditions for the winter months in Denmark.

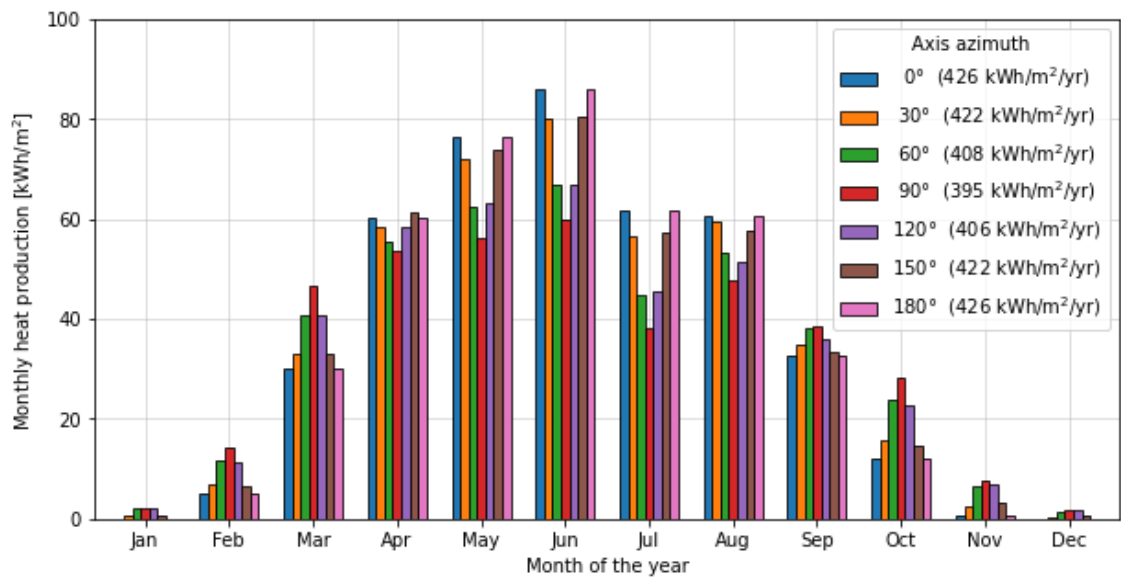


**Figure 20:** Monthly heat production for different azimuth orientations. Row spacing = 15 m.

To summarize, it was shown that the thermal performance increased with increasing row spaces, though with limited effect for row spacings greater than 20 m. Also, the optimal axis azimuth was found to be with the tracking axis aligned North-South. Though for the configuration in Brønderslev with 29.9° north of south, the performance was reduced by less than 1% compared to a North-South tracking axis. In contrast, the difference between the optimum (0°) and the worst orientation (90°) was 7%.

Eventually, the choice of configuration parameters is an economic decision, which depends on the local land prices and the available land geometry. E.g., for places with higher land prices, the optimal row spacing will be shorter than for places with lower land prices.

## References

- [1] Brønderslev Forsyning, "Principskitser." [Online]. Available: <https://www.bronderslevforsyning.dk/varme/solvarme-og-biomasseanlaeg/principskitser/>. [Accessed: 14-Dec-2020].
- [2] Solutia, "Therminol 66 High Performance Highly Stable Heat Transfer Fluid - Group Provoc T.B.S 10-7 (12/98) E." .
- [3] F. Sallaberry *et al.*, "Evaluation of the tracking accuracy of parabolic-trough collectors in a solar plant for district heating," *AIP Conf. Proc.*, vol. 2033, November, 2018.
- [4] IEC, "IEC 62862 Part 3-2 : Systems and components – General requirements and test methods for large-size parabolic-trough collectors." 2018.
- [5] ISO, "ISO 9806:2017 Solar energy-Solar thermal collectors-Test methods," 2017.
- [6] L. Valenzuela, R. López-Martín, and E. Zarza, "Optical and thermal performance of large-size parabolic-trough solar collectors from outdoor experiments: A test method and a case study," *Energy*, vol. 70, pp. 456–464, 2014.
- [7] F. Burkholder, "Heat loss test results for the Huiyin-group receiver," 2012.
- [8] B. Perers, "Verification of high temperature performance for the 0.8 MW CSP test plant at Brønderslev," 2015.
- [9] F. Sallaberry, Z. Tian, B. Perers, S. Furbo, A. Zourellis, and J. H. Rothmann, "On-site parabolic-trough collector characterization in solar district heating plant under quasi-dynamic conditions," *AIP Conf. Proc.*, vol. 2126, July, 2019.
- [10] F. Sallaberry, L. Valenzuela, and L. G. Palacin, "On-site parabolic-trough collector testing in solar thermal power plants: Experimental validation of a new approach developed for the IEC 62862-3-2 standard," *Sol. Energy*, vol. 155, pp. 398–409, 2017.
- [11] S. A. et al Klein, "TRNSYS 18: A Transient System Simulation Program." Solar Energy Laboratory, University of Wisconsin, Madison, USA, 2017.
- [12] National Renewable Energy Laboratory, "System Advisor Model Version 2017.9.5 (SAM 2017.9.5)." [Online]. Available: <https://sam.nrel.gov/download>.
- [13] Z. Tian, B. Perers, S. Furbo, and J. Fan, "Annual measured and simulated thermal performance analysis of a hybrid solar district heating plant with flat plate collectors and parabolic trough collectors in series," *Appl. Energy*, vol. 205, August, pp. 417–427, 2017.
- [14] Z. Tian, B. Perers, S. Furbo, and J. Fan, "Thermo-economic optimization of a hybrid solar district heating plant with flat plate collectors and parabolic trough collectors in series," *Energy Convers. Manag.*, vol. 165, October 2017, pp. 92–101, 2018.
- [15] B. Ahlgren *et al.*, "A simplified model for linear correlation between annual yield and DNI for parabolic trough collectors," *Energy Convers. Manag.*, vol. 174, July, pp. 295–308, 2018.
- [16] S. A. et al Klein, "TRNSYS 18 a TRaNsient SYstem Simulation program - Volume 4: Mathematical Reference," 2017.



BYG R-449  
December 2020

ISBN: 87-7877-550-7

Department of Civil Engineering, DTU  
Brovej, Building 118  
2800 Kgs. Lyngby

[www.byg.dtu.dk/english](http://www.byg.dtu.dk/english)  
Tel: 4525 1700